Photoacoustics 29 (2023) 100456

Contents lists available at ScienceDirect

Photoacoustics

journal homepage: www.elsevier.com/locate/pacs

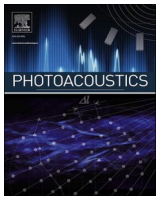

Efficient label-free *in vivo* photoacoustic imaging of melanoma cells using a condensed NIR-I spectral window

Soon-Woo Cho [a], Thi Tuong Vy Phan [b,c], Van Tu Nguyen [d], Sang Min Park [e], Hwidon Lee [f,g], Junghwan Oh [h,i,*], Chang-Seok Kim [a,e,**]

[a] *Engineering Research Center for Color-modulated Extra-sensory Perception Technology, Pusan National University, Busan 46241, the Republic of Korea*
[b] *Center for Advanced Chemistry, Institute of Research and Development, Duy Tan University, Danang 550000, Viet Nam*
[c] *Department of Environmental and Chemical Engineering, Duy Tan University, Danang 550000, Viet Nam*
[d] *Department of Biomedical Engineering, Duke University, Durham, NC 27708, USA*
[e] *Department of Cogno-Mechatronics Engineering, Pusan National University, Busan 46241, the Republic of Korea*
[f] *Harvard Medical School, Boston, Massachusetts MA 02115, USA*
[g] *Wellman Center for Photomedicine, Harvard Medical School and Massachusetts General Hospital, 40 Blossom Street, Boston, MA 02114, USA*
[h] *Department of Biomedical Engineering, Pukyong National University, Busan 48513, the Republic of Korea*
[i] *Ohlabs Corporation, Busan 48513, the Republic of Korea*

ARTICLE INFO

Keywords:
Photoacoustic microscopy
Melanoma
Fiber laser
High-speed
Near-infrared
Nonlinear effect
Stimulated Raman scattering
Supercontinuum

ABSTRACT

In this paper, we propose an efficient label-free *in vivo* photoacoustic (PA) imaging of melanoma using a condensed near infrared-I (NIR-I) supercontinuum light source. Although NIR-II spectral window is advantageous such as longer penetration depth compared to the NIR-I region, supercontinuum light sources emitting both NIR-I and NIR-II region could lower the efficiency to target melanoma because of low optical power density in the melanoma's absorption spectra. To exploit efficient *in vivo* PA imaging of melanoma, we demonstrated the light source emitting from visible (532–600 nm) to NIR-I (600–1000 nm) by optimizing stimulated Raman scattering induced supercontinuum generation. The melanoma's structure is successfully differentiated from blood vessels at a high pulse energy of 2.5 μJ and a flexible pulse repetition rate (PRR) of 5–50 kHz. The proposed light source with the microjoules energies and tens of kHz of PRR can potentially accelerate clinical trials such as early diagnosis of melanoma.

1. Introduction

Melanoma is a fetal cancer that develops from the melanocytes that are found predominantly in the skin. Although malignant melanoma can be surgically treated in the early stage with a success rate of 80%, it is still challenging to treat it after the metastatic stage [1]. Therefore, innovative clinical technologies are required for the early diagnosis and/or prognosis of melanoma. In the past, invasive excisional or incisional biopsies were mainly performed in clinical practice for early diagnosis of melanoma which can damage even healthy skin and leave behind scars. To overcome biopsies' invasibility and improve the accuracy of diagnosis, various noninvasive imaging techniques have been demonstrated such as dermoscopy [2,3], reflectance confocal microscopy (RCM) [4,5], and optical coherence tomography (OCT) [6,7]. Dermoscopy, the most traditional method, is highly dependent on the operators' perspective with subjective interpretation requiring sufficient training, therefore, additional meta-analysis is inevitable for objective diagnosis [8]. Although the RCM and the OCT are relatively recent methods, they have low penetration depth according to their pure optical properties [9] and have a drawback in perspectives of molecular selection.

Photoacoustic (PA) technique has also been suggested as a competitive noninvasive tool for monitoring the blood vessels and tumor-targeted agents owing to its potential in cellular and molecular-specific imaging [10–13]. Because the optical energy deposition related to optical absorption coefficients is proportional to the

* Corresponding author at: Department of Biomedical Engineering, Pukyong National University, Busan 48513, the Republic of Korea.
** Corresponding author at: Engineering Research Center for Color-modulated Extra-sensory Perception Technology, Pusan National University, Busan 46241, the Republic of Korea.
E-mail addresses: jungoh@pknu.ac.kr (J. Oh), ckim@pusan.ac.kr (C.-S. Kim).

https://doi.org/10.1016/j.pacs.2023.100456
Received 7 December 2022; Received in revised form 25 January 2023; Accepted 25 January 2023
Available online 27 January 2023

magnitude of the PA signal, the multiple pigments can be distinguished by varying the wavelength of excitation laser. In the circulating tumor cells (CTCs) test, which is an alternative to assaying lymph nodes or bone marrow, the PA technique enables distinguishing melanoma from the blood to improve the test sensitivity. This technique (so-called photoacoustic flow cytometry) has been consistently reported for monitoring metastatic melanoma cells [14–19]. In addition to CTCs, PA imaging of subcutaneous melanoma has been demonstrated both *ex vivo* [20–22] and *in vivo* studies [23–29].

Although the PA images of melanoma can be obtained with a single wavelength at the visible or NIR range, it is difficult to differentiate melanoma from the blood vessels with a single laser. With a visible laser, high background PA signals from blood vessels interfere the high-contrast melanoma image. Also, a single wavelength in the NIR-I region can image the melanoma, however, surrounding blood vessels cannot be obtained. Therefore, the dual spectral band [23,24] or dual single wavelength laser [30] have been required to enhance the sensitivities by distinguishing between the melanoma and the blood vessels. Even though the NIR-II (1000–1700 nm) has a deeper penetration according to the reduced photon scattering compared with the visible (*e.g.*, 532–600 nm) or the NIR-I spectral region (*e.g.*, 600–1000 nm) [31], the NIR-I window can be potentially the best optical window considering melanoma's optical absorption having enough penetration depth in biomedical tissue [32,33]. Therefore, for an efficient manner, pulsed light source emitting a 532–1000 nm spectral band could have potentially the best performance for the simultaneous PA measurements of the blood vessels and the melanoma.

PA techniques of melanoma detection have gradually developed aiming at clinical applications such as hand-held [28,29,34] and various PA modalities [35,36], but it is still suffered from a slow imaging speed and efficient spectral bands. In PA technologies, the imaging speed is essentially limited by the pulse repetition rate (PRR) of the light source. Several kinds of pulsed light sources have been used for melanoma detection. Conventional bulk solid-state lasers have a slow PRR below 1 kHz generally because the average threshold power of pump light increases linearly with PRR causing degradation of the optical parametric oscillator's (OPO) performance by the thermal effect [37,38]. Ultimately, since the PA technique aims to be translated into clinical application, the research of fully integrated PAM [39–41] and high-speed PAM [42–47] have been actively progressed. Fiber-based light sources such as the supercontinuum (SC) sources [48–59] and stimulated Raman scattering source (SRS) sources [60–69] have been suggested for high-speed multispectral or functional PA imaging. The nonlinear effect can be maximized at a relatively low pump threshold power owing to the advantages of the nonlinear effective length and effective area with an optical fiber-based configuration [70]. Thus, the broadband spectrum can be implemented using a microchip laser or diode-pumped fiber laser (μJ scale of pulse energy at hundreds of kHz of PRR) instead of using a bulk solid-state laser (mJ scale of pulse energy at tens of Hz). However, the extremely broad spectrum of the SC light sources causes lower energy density in the NIR-I spectral region causing lower PA signals from the blood vessels and the melanoma. Thus, *in vivo* functional melanoma PA imaging has been so far challenging due to the lack of a light source having high energy density and PRR in the NIR-I spectral window.

Fig. 1 represents the necessity of a condensed NIR-I SC source. The absorption coefficient spectra of endogenous agents to be considered for *in vivo* PA imaging of melanoma are shown in the upper graph. Since the absorption peaks of oxy- and deoxyhemoglobin (at normal concentrations in blood, *i.e.*, 150 gL^{-1}) are in the visible region, melanin has relatively higher absorption in the NIR-I region so that melanoma can be efficiently differentiated from around blood vessels. In the NIR-II region, the absorption coefficient of melanin continues to decrease, but the water absorption coefficient gradually increases, interrupting targeting melanoma. Even though conventional ultra-broadband SC source includes NIR-I spectral band, their extremely broad spectrum causes the lower optical power distribution in that range.

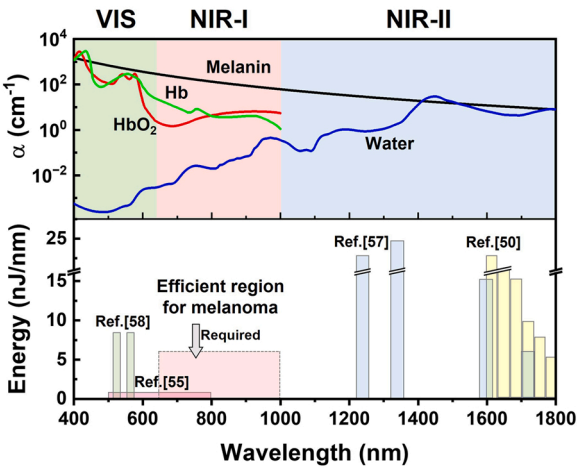

Fig. 1. Necessityof light source with a condensed NIR-I energy for efficient *in vivo* PA imaging of melanoma. Absorption coefficient spectra of melanin (black) [71], oxyhemoglobin (red), deoxyhemoglobin (green) [72], and water (blue) [73] are represented in the upper graph. α, absorptioncoefficient. In the lower graph, the energy spectral diagram of SC source for *in vivo/in vitro* PA studies in the literature is schematized [50, 55, 57, 58].

In the lower graph in Fig. 1 shows the energy spectral diagram of SC sources filtered by bandpass filter for *in vivo/in vitro* PA experiment. Dasa et al. [50] developed the high-pulse energy SC source ranging for multi-spectral PAM imaging of lipids. They demonstrated the six excitation bands (1650–1850 nm) by performing *in vivo* Xenopus laevis tadpoles with a pulse energy of 4–22 nJ/nm. Buma et al. [57] performed the multispectral OR-PAM of a fixed Drosophila larva using SC source with the spectrum of 1050–1714 nm. Although the energy at 1050 nm is highest over ~6 μJ, the low absorption coefficient of lipids causes poor image contrast. The efficient spectral energy band of lipids ranging from 1225 to 1714 nm was 6–24 nJ/nm. These two groups adapted the pulse energy of several nJ/nm at least for *in vivo* PA studies. Shu et al. [55] adapted the SC light to the combine PAM and OCT. The output optical power filtered from 500 to 800 nm was 3 mW at a PRR of 25 kHz, which is corresponding to 0.4 nJ/nm for *in vivo* mouse ear and *ex vivo* porcine blood. Chang et al. [58] performed the multispectral PAM and OCT, also. The visible band (500–600 nm) is used for functional PAM. Even though *in vivo* PA imaging of melanoma was achieved, the melanoma was imaged together with blood vessels with similar PA intensity in transmission mode OR-PAM. Therefore, a light source that has NIR-I spectral window with sufficient pulse energy is required to avoid the strong absorption spectrum of hemoglobin and water for efficient melanoma imaging.

In this study, we propose a NIR-I SC source can efficiently differentiate melanoma from the background tissues (*e.g.*, blood vessels) in *in vivo* PA imaging. We first performed a phantom study with photothermal agents fabricated nanoparticles (NPs) to confirm the feasibility of the proposed NIR-I SC source. For the *in vivo* study, melanoma cells were subcutaneously injected into the mouse and demonstrated the label-free melanoma imaging with 5 kHz A-line rate. Photoacoustic microscopy (PAM) using an NIR-I SC source can offer a novel opportunity for high-speed *in vivo* PA imaging and early detection of skin cancer (*e.g.*, melanoma) with pulse energy of several μJ. Recently, deep learning methods have been actively applied to biomedical PA imaging field to facilitate the clinical translation [74,75]. With this potential research environment, it is promising that identifying the accurate lesion size and location surrounded by blood vessels will be helpful in tumor staging diagnosis. We expect that its simple configuration, high-speed (over 5 kHz), and optimized energy (~ 2.5 μJ) within the NIR-I range can accelerate clinical trials for early diagnosis of melanoma.

2. Material and methods

2.1. Optimization of a condensed NIR-I SC source

To simultaneously image blood vessels and melanoma with a single light source, an optimization process was performed, as shown in Fig. 2 (a). Since the spectra of the visible region for hemoglobin and the NIR-I region for melanoma are required, the wavelength of the pump source (λ_{pump}) was selected as 532 nm, the most common in the visible region. And, for red-shift to the NIR-I region, a normal dispersion regime (Fig. 2 (b)) that dominantly causes the cascaded SRS effect was adopted instead of the anomalous dispersion regime which is generally used to implement SC generation. That is, the case that λ_{pump} is shorter than the zero-dispersion wavelength (λ_{ZDW}) so that the dispersion (D) of the optical fiber is negative. Note that λ_{ZDW} is the wavelength where no group delay dispersion occurs, which is determined by the material and structure of the optical fiber. Therefore, we planned to adopt the normal dispersion fiber (NDF), which has λ_{ZDW} longer than 532 nm and effective area (A_{eff}) larger tens μm^2 (Photonic crystal fiber used in ultra-broad SC generation has extremely small A_{eff} and core diameters down to 1 μm [76]). The main factors affecting the SRS effect in optical fiber are represented in Fig. 2(c)). In addition, considering the Raman threshold pump power (P_{th}) can be approximated at $\sim 16 A_{eff} k_p^{-1} L_{eff}^{-1} g_r^{-1}$ [70], low concentration GeO_2 doped silica was considered as the fiber core material regarding the Raman gain coefficient (g_r). This is because fibers doped with oxide glasses with high g_r can form sharp Raman Stokes up to λ_{ZWD} due to the extremely efficient SRS effect. It was reported that the sharp SRS stokes were generated up to 1320 nm (near the λ_{ZDW}) by using a 523 nm pump source with a 1 km of higher concentration GeO_2-doped silica fiber ($g_r = 2.9 \times 10^{-13}$ mW^{-1} @523 nm) [77]. Similarly, since we designed the broadened SC generation in the NIR-I region, non-polarization maintaining fiber (Non-PMF) was chosen. The randomly changing polarization of the signal and pump wave causes the polarization factor (k_p) to decrease. This effect also suppresses the extremely efficient SRS by increasing the P_{th}. As a NDF that satisfies all of these requirements, standard single mode fiber (SMF-28, 3.6 mol% GeO_2, $A_{eff} = \sim 85$ μm^2) was finally adopted, after then, the optimization of fiber length was progressed. First, the ratio of NIR-I spectrum energy density (R_{NIR-I}) to the full spectrum was required to be greater than the visible spectrum (R_{VIS}) ratio. After then, the longest shifted wavelength (λ_{max}) was aimed to reach 1000 nm. Fig. 2(d) shows the full spectrum of NIR-SC source at the NDF's lengths of 30 m, 50 m, and 100 m. Due to the SRS seeds the SC growth [78], the output spectra show different aspects compared with the typical SC source (or SRS source) used in the previous PA studies. We could observe that the longer the effective area, the weight of the NIR-I spectrum increased. At the NDF's length of 100 m, the spectral broadening finally occurred up to 1000 nm. Considering the NIR-I energy and the potential for imaging depth improvement, we selected a 100 m-NDF. This feature can benefit for distinguishing the blood vessels and melanoma cells because both the energy distributions of the visible lights and NIR-I range are sufficient for *in vivo* PA imaging.

2.2. Experimental setup

Fig. 3(a) presents a schematic diagram of the PAM system using NIR-I SC source for label-free melanoma imaging. A Q-switched Nd:YAG microchip laser (SPOT-10–100–532, Elforlight), which was operated with a flexible PRR of 5–50 kHz at 1.8 ns pulse duration. The output beam was collimated and refocused by using a 1:1 magnification achromatic doublet pair (AC127–025-AB, Thorlabs). To filter the NIR-I spectrum, the long-pass filter (FGL610H, Thorlabs) was installed by a motorized filter wheel between the fiber-end and lens pair. The focused beam was excited and then was aligned confocally using a focused transducer with a center frequency of 25 MHz through an optical/acoustic combiner (OAC). For volumetric imaging of the target, a two-axis linear stage was used by performing a zigzag scan along the x-y plane. During the imaging, the PRR of the light source was set to 5 kHz according to the low scanning speed of the linear stage. The image speed can be further improved by using a high-speed galvanometer scanner [79], a polygon mirror scanner [80], or slider-crank scanner [81]. Also, there is room for further improvement of the imaging efficiency by using the optical fiber delay or a high-speed optical filter to illuminate the dual spectral band with a single scanning. The generated PA signals were then amplified and acquired using two serially connected amplifiers and using a digitizer with a bandwidth of 100 MHz, respectively.

By applying the optimization study, a fiber length of 100 m was

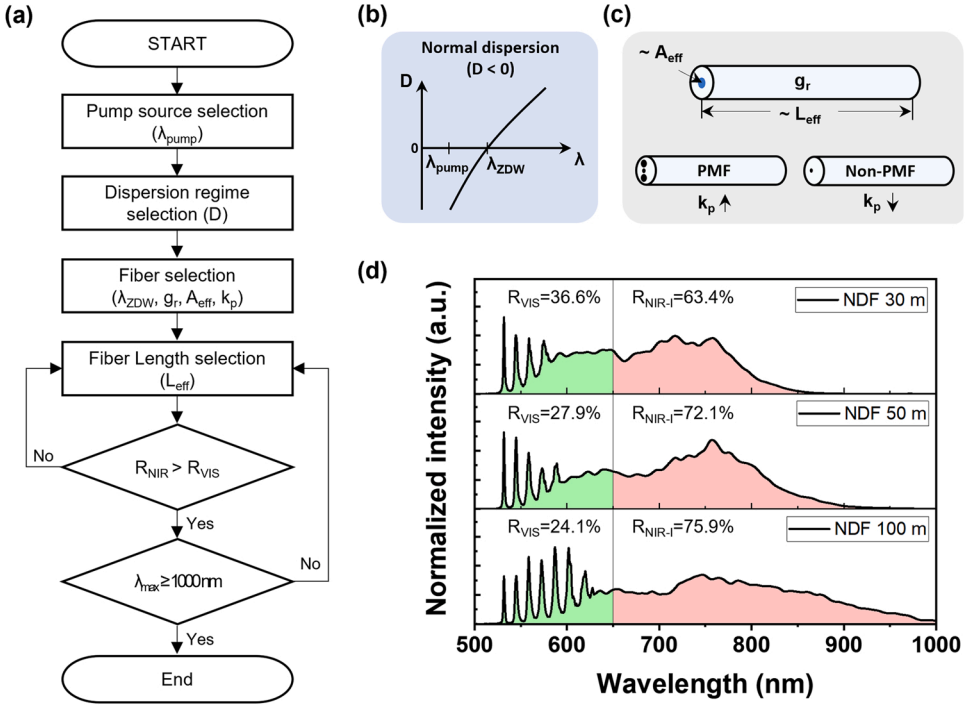

Fig. 2. (a) Optimization process flowchart of a condensed NIR-SC source. (b) Dispersion curve diagram in normal dispersion (D < 0). (c) Main factors affecting SRS effect in the optical fiber. (d) The full spectrum of NIR-SC source at the NDF's lengths of 30 m, 50 m, and 100 m. The visible region (500-650 nm) is colored light green, and the NIR-I region (650-1000 nm) is pink. λ_{pump}, wavelength of pumpsource; λ_{ZDW}, zero dispersion wavelength of the fiber; λ_{max}, the longest shifted wavelength; D, dispersion; g_r, Raman gain coefficient; A_{eff}, effective core area; k_p, polarization factor; L_{eff}, effective length; $R_{VIS/NIR-I}$, the ratio of visible/NIR-I spectrum energy density to the full spectrum.

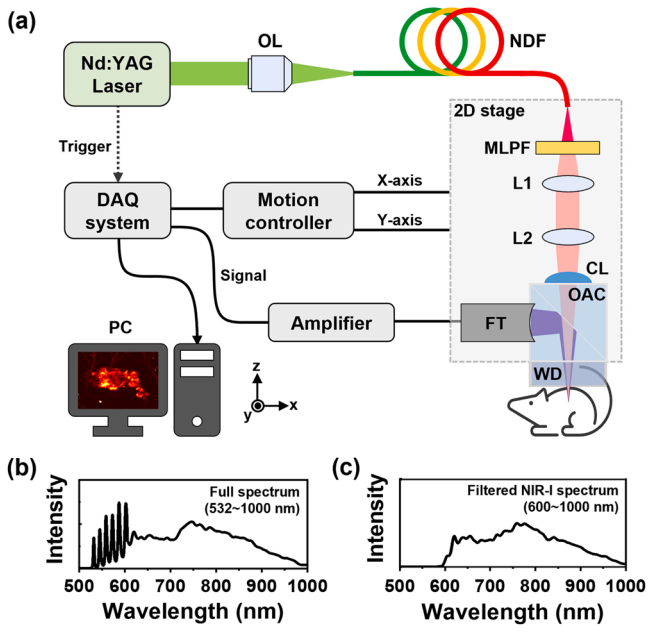

Fig. 3. (a) Schematic of the PAM system using NIR-I SC source. (b) Full spectrum and (c) the filtered NIR-I spectrum used for PA imaging. OL: Objective Lens; NDF: Normal Dispersion Fiber; MLPF: Motorized Long-Pass Filter; L1–2: Achromatic Lenses; CL: Corrective Lens; FT: Focused Transducer; WD: Water Dish; DAQ: Data Acquisition; OAC: Optical/Acoustic Combiner.

selected to perform *in vivo* PA experiment. As shown in Fig. 3(b), the entire spectrum of the proposed NIR-I SC source emits the light from 532 nm to 1000 nm showing multi-discrete SRS wavelengths in the visible region (532, 545, 558, 572, 587, 603 nm) and broad NIR-I continuum spectrum (600–1000 nm). Note that we used the entire spectrum for the blood vessel imaging to maximize PA signals, since it has a broad optical absorption through the visible to NIR-I spectral window. Further, the *in vivo* PA image of the melanoma's structure was differentiated using only the NIR-I spectrum (Fig. 3(c)) filtered by a long-pass filter (cut-off at 600 nm) to minimize PA signals from the blood vessels. Both the spectra were measured with the compact CCD spectrometer and the maximum pulse energy of the full and the filtered NIR-I spectra were measured to be 3.4 μJ and 2.5 μJ, respectively.

3. Results

3.1. Phantom study

To demonstrate the feasibility of the proposed NIR-I SC source, we first performed a phantom study using the hyaluronan-stabilized iron-platinum nanoparticles (FePt@HA NPs) as NIR-I photothermal agents, which exhibit similar absorption characteristics similar to melanin. Fig. 4 shows the *in vitro* evaluation of the photothermal agents using an optimized source. Fig. 4(a) shows the top-view image of the phantom and the corresponding PA image acquired using the NIR-I SC spectrum. Six phantom samples were filled with pretreated cancer cells; five samples contain different concentration of FePt@HA NPs (12.5, 25, 50, 100, and 200 μg/ml) and the rest of sample was mixed with 4% gelatin only. As shown in Fig. 4(b), the amplitude of the PA signal increased with an increasing concentration NPs, depicting the potential of the NIR-I SC source to act as an excitation laser for NP-mediated photothermal therapy (PTT) in conjunction with photothermal agents such as the FePt@HA NPs. For a more practical demonstration, *in vivo* PA experiment was also performed (see supplement Fig. S1), which also indicates that the NIR-I SC source can potentially monitor photothermal agents for PA imaging-guided PTT [82].

3.2. Label-free PA imaging of melanoma tumor

This study aimed to demonstrate melanoma imaging using the proposed NIR-I SC source. Thus, we first performed am *in vitro* experiment on melanoma cells placed on a glass dish to measure their sizes and melanin concentrations. As shown in the optical microscopy (OM) image (Fig. 5(a)), the cell size of a single melanoma (SM) has a wide range (10–30 μm diameter). The corresponding PA image (Fig. 5(b)) clearly shows the melanoma cell distribution as well as the melanin excretion by melanoma cells. The melanin concentration can be estimated using the PA signal amplitudes, and we confirmed that. There were 15-fold variations in melanin concentrations among the melanoma cell samples from the results. The PA signals were not observed from the non-pigmented melanoma cells, regardless of the concentration of melanoma cells, because of the non-absorption of light by the non-pigmented melanoma cells.

Fig. 6 presents *in vivo* functional optical-resolution photoacoustic microscopy (OR-PAM) images of subcutaneous melanoma distribution and the surrounding blood vessels in the mouse skin. MAP PA images (Figs. 6(b) and 6(c)) were acquired at a PRR of 5 kHz for 5 min. The scanning step sizes were 2 μm and 40 μm along the x and y directions. As shown in Fig. 6(b), both morphological information of melanoma and blood vessels were detected simultaneously because both hemoglobin and melanin have substantial strong absorption in this spectral range. Micro-vessels with diameters of less than 40 μm (20 pixels), presumably resulting from angiogenesis, can be observed to surround the melanoma. Fig. 6(c) shows the morphology of melanoma clearly by using the filtered NIR-I spectrum (600–1000 nm) because of the minimal optical absorption of blood vessels. Melanoma occupies an area of approximately 22 mm^2 in the PA image with field of view (FOV) of 10 × 10 mm^2. Fig. 6(d) represents the superposition of two PA images of Fig. 6(b) and (c); thereby, clearly distinguishing the melanoma and its surrounding vasculature. As shown in Fig. 6(e), the 3D volumetric PA image can be also acquired (10 × 10 × 0.9 mm^3) from the data set of

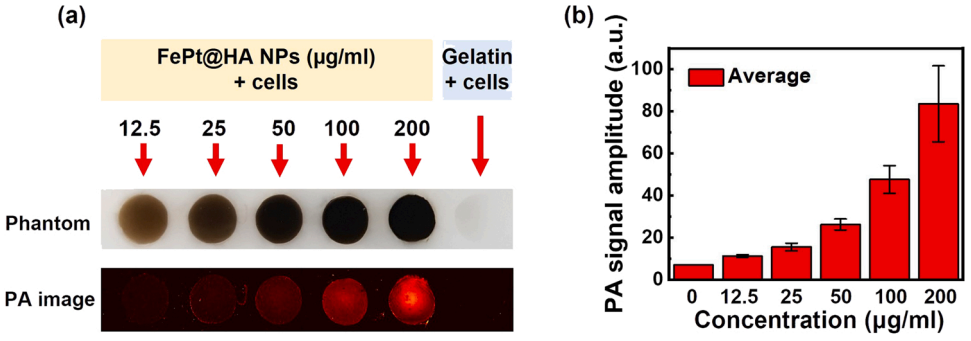

Fig. 4. *In vitro* PA imaging of photothermal agents (FePt@HA NPs) using NIR-I SC source. (a) Phantom and corresponding PA images at various concentrations. (b) Evaluation of PA signal response corresponding to each concentration.

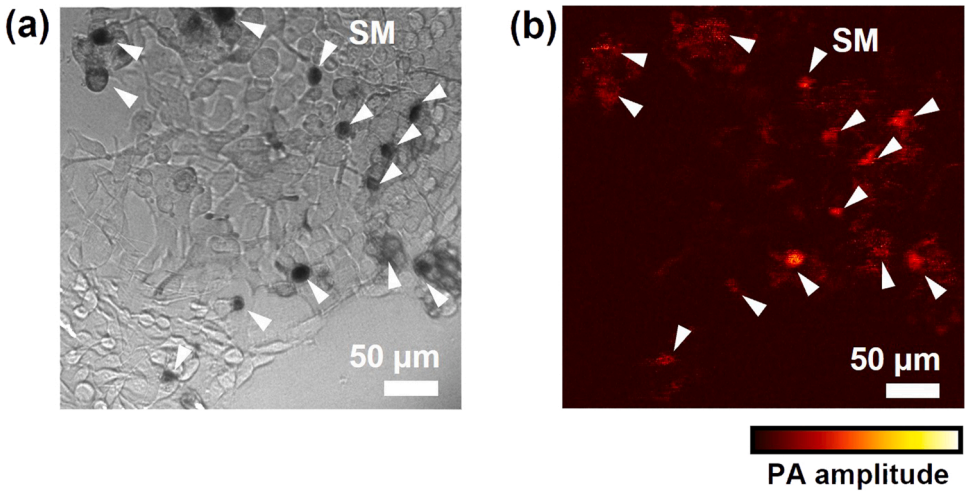

Fig. 5. PA monitoring of B16 melanoma cells *in vitro*. (a) Optical microscopy (OM) image (b) MAP PA image. Single melanoma (SM).

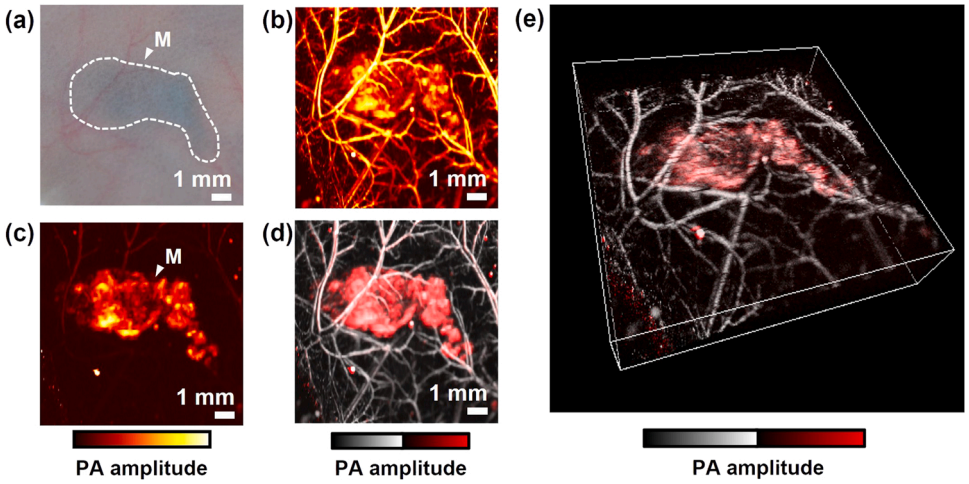

Fig. 6. *In vivo* PA images of a subcutaneously inoculated B16-melanoma in an immunocompromised nude mouse (on the back). (a) Photograph of the melanoma. MAP image of the blood vessels and melanoma cells at (b) the full spectrum and (c) the filtered NIR-I spectrum. (d) Superposition of two MAP PA images ((b) is colored in gray and (c) is colored in red). (e) 3D volumetric PA image acquired from the data set of (d).

Fig. 6(d) using 3D Photoacoustic Visualization Studio (3D PHOVIS) software [83].

At the full spectrum, the average ratio of the melanoma to the background is 16.94 ± 0.70, and the average ratio of melanoma to the surrounding blood vessels is 0.98 ± 0.03 in PA signal amplitude. Thus, the difference in PA signal amplitude of melanoma and the blood vessels is not very significant, which makes it difficult to differentiate them. Using only the NIR-I spectrum, the average ratio of the melanoma to the background is still maintained at 16.61 ± 0.73, whereas the average ratio of the melanoma to the blood vessels is enhanced to 6.29 ± 0.88 (~ 6 times higher). Therefore, the melanoma can be distinguished from its surrounding vasculature and visualized according to their different absorption spectra using dual-band excitation; thereby, enabling the estimation of the melanoma tumor distribution. This result demonstrates that OR-PAM using the proposed NIR-I SC source can efficiently detect and evaluate melanoma.

Further, we performed continuous cell tracking over a week to monitor melanoma migration and proliferation. To verify the noninvasive *in vivo* melanoma monitoring, the label-free B16 melanoma cells were longitudinally visualized using OR-PAM. The mouse ear is considered to be a sufficient model for validating the system due to its similarity with the human skin and lack of motion artifacts [84]. As shown in Fig. 7(a)-(c), PA images with FOV of 13 × 7 mm^2 area are acquired at a PRR of 5 kHz. The scanning step sizes were 2 and 20 μm in the x, y directions, respectively. B16 melanoma cells were injected subcutaneously into the left ear of the mouse and imaged on day 3 and 10 using the NIR-I SC source in two spectral regions: in the full spectrum (532–1000 nm) and in the NIR-I spectrum (600–1000 nm). The result of spectral analysis in NIR spectrum illumination differentiates melanoma cells from other tissue components. All the OR-PAM images in Fig. 6 are composites of the two MAP images within these two spectral ranges. The spatial distribution of label-free melanoma (yellow bar), was quantified on day 3 and 10 after the injection, respectively. On day 3, melanoma cell signals were prominently observed in the PA image. The SNR of the melanoma tumor region was 22 dB on day 3, and the tumor size was approximately 4 mm^2. On day 10, the PA signals from the melanoma cells were diminished compared to those on day 3. The SNR of the melanoma tumor region decreased to 16 dB. Fig. 7(d) shows quantitative analysis of *in vivo* PA imaging results. The spatial positions of the PA signals obtained from melanoma cells were summed and displayed as yellow bar. Moreover, PA signals from the background were referred to in the gray bar as the control group. The total PA signal amplitude of melanoma cells decreased by 2-fold while those of the background tissues remained in the same values. Because the PA signal is proportional

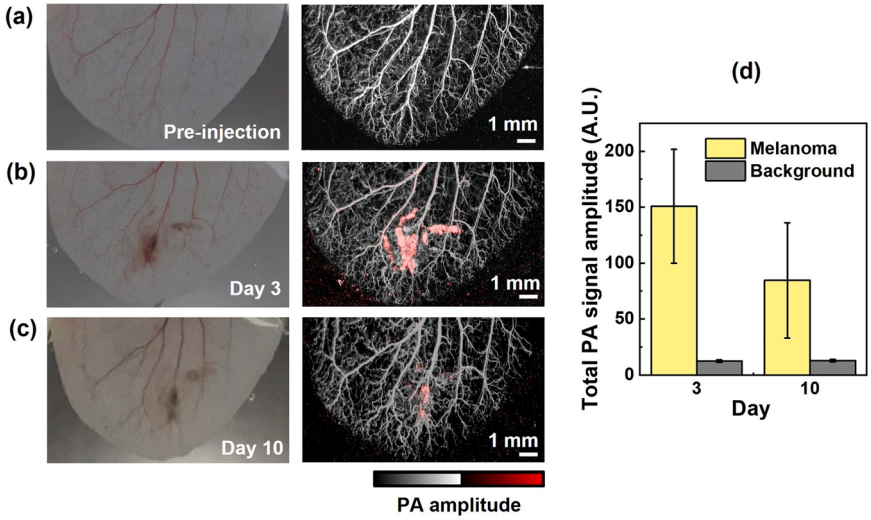

Fig. 7. Monitoring the growth of melanoma before and after injection of B16 melanoma cells. (Top) Photographs and (Bottom) corresponding OR-PAM images. (a) Before injection. (b) After injection of B16 melanoma cells on day 3 and (c) day 10. (d) Quantitative analysis of PA signals obtained from the melanoma cells.

to the concentration of melanoma cells, half of the melanoma cells were estimated to have undergone cell death on the period of days 3–10. Through the experimental results, the feasibility of non-invasive *in vivo* monitoring of label-free melanoma cells has been shown with a capability to quantify the melanoma cells with high sensitivity using the proposed NIR-I SC source.

4. Discussion

Over the last decade, nanosecond pulsed SC sources have been proposed for PA imaging [48–58] (see supplement Table S1). Some SC sources have been developed as OCT detection lasers in the combined PAM and OCT system owing to their broadband properties [49,55,56,58]. However, in this study, we focused on developing the light source for PA excitation.

Majority of the SC studies have reported using anomalous dispersion regime (positive dispersion) with highly nonlinear fiber to efficiently generate a broader continuum spectrum [85]. In particular, the combination of a 1064 nm pump laser and photonic crystal fiber (PCF) with λ_{ZDW} at 1047 nm or 1060 nm has been generally used in multispectral PA studies. Multispectral property of the SC effect is utilized for spectral PA measurement in various spectral regions, for instance, the hemoglobin concentration and oxygen saturation were sensed photoacoustically with an extracted visible lights (530 and 610 nm) [51] and multispectral PAM (*i.e.*, blood, lipid) was performed using filtered visible to NIR-I spectrum (500–800 nm) [55] and NIR-II (1050–1714 nm) [57] spectral windows. However, the ultra-broadband spectrum, extending from 400 to 2400 nm, can make it difficult to achieve condensed pulse energy in a specific wavelength region of interest especially for the melanoma detection. In 2015 and 2018, Ferrari et al. [52] and Buma et al. [57] reported a continuum spectrum for PA imaging with a normal dispersion regime using a pump wavelength below the λ_{ZDW} of the optical fiber. In both the output spectra, the SRS effect occurred predominantly at the beginning and continuum induced by four-wave-mixing (FWM) appeared to gradually shift toward the red-end with an increasing incident pump energy.

To confine the fiber-coupled energy to a specific NIR-I spectral window (600–1000 nm), we selected the normal dispersion regime (λ_{pump}-λ_{ZDW} <0, negative dispersion). The fiber had a longer λ_{ZDW} (*i.e.*, 1310 nm) than λ_{pump} (*i.e.*, 532 nm). Thus, the pump wavelength lies in the normal dispersion region of the fiber waveguide where there is no nonlinear phase-matching. Using the pump lights with ultrashort pulses (10–100 fs) having a high peak power of over 10 MW, SC generation induced by self-phase modulation (SPM) tends to lead dominantly [86]. When pumping with an ns pulse, the SPM is negligible, and both the SRS and the parametric FWM effects dominate in optical fiber [87]. The FWM gain can be broadened because of the parametric pump photons near λ_{ZDW}. The rapid spectral broadening of the Raman orders of the pump is estimated because of the integrated impact of modulation instability and the soliton effects [88]. Based on these studies, we focused on the characteristic of asymmetric spectral broadening to attain the desired energy value because the energy distribution in the region of interest (especially the NIR-I region) is a critical requirement in subcutaneous melanoma imaging.

This study demonstrated, for the first time, both *in vivo* PA monitoring of melanoma cells and blood vessels at several kHz by emitting visible and NIR-I spectral bands. The optical absorption of melanin in the NIR-I spectral range (600–1000 nm) is efficient for the generation of highly sensitive PA images of melanoma tumors from surrounding blood vessels. We monitored melanoma cells over a long period (over 1 week) and demonstrated the feasibility of NIR-I light source in the *in vitro* and *in vivo* experiments. Because other optical imaging modalities have their own drawbacks such as the perspective of operators (dermoscopy) and limited molecular selection (RCM, OCT), *in vivo* PA imaging of label-free melanoma cells can provide various advantages simultaneously (depth-resolved imaging, cell tracking ability, high sensitivity to the surrounding blood vessels and background tissue). Therefore, a PAM system equipped with a high-speed NIR-I SC source can propose a potential to enhance the imaging speed for clinical trials of melanoma imaging. To contribute to the clinical translation, our future efforts will focus on developing a high-energy light source with several tens of microjoules for human melanoma imaging, which would be demonstrated in the AR-PAM system.

5. Conclusion

We demonstrated the efficient label-free *in vivo* PA imaging of melanoma cells and blood vessels simultaneously using a high-speed NIR-I SC source. The key features are (1) condensed energy density in NIR-I spectral region (for melanoma imaging), (2) high pulse energy of up to 3.4 μJ at 532–1000 nm (2.5 μJ at 600–1000 nm), (3) high repetition rate, and (4) fiber-based simple system implementation. Here, we focused on emitting the SC light source cut-off at 1000 nm wavelength which can effectively target the melanoma cells rather than ultrabroad continuum generation even covering NIR-II spectral region. The imaging speed can be further increased using the proper light scanning system

such as a galvanometer scanner and polygon mirror scanner. The proposed light source aiming for label-free subcutaneous melanoma imaging was conducted with a simple microchip laser at 532 nm with a cost effective NDF. We expect that these advantages contribute to high-speed melanoma detection with high sensitivity for preclinical and clinical trials.

Author contribution

S.-W. Cho designed and optimized the NIR-I SC source, performed *in vivo* experiments, prepared the figures, and wrote the manuscript. T.T.V. Phan synthesized the nanoparticles and prepared the *in vivo* experiments. V. T. Nguyen developed the OR-PAM system and performed *in vitro* experiments. S.M. Park prepared the light source and experimental system. H. Lee interpreted the data and revised the manuscript. C.-S. Kim and J. Oh supervised the project and approved the final version. All authors contributed to the critical reading of the manuscript.

Declaration of Competing Interest

The authors declare no conflicts of interest.

Data Availability

Data will be made available on request.

Acknowledgement

This research was supported by the National Research Foundation of Korea (NRF) grant funded by the Korea government (MSIT) (No. 2021R1A5A1032937, No. 2022R1A5A8023404, 2022R1C1C2010976), and the Korea Medical Device Development Fund (KMDF) grant funded by the Korean government (MSIT, MOTIE, MOHW, and MFDS) (202011C13, KMDF_PR_20200901_0055). It was also supported by the Korea Evaluation Institute of Industrial Technology (KEIT) grant funded by the Korea government (MOTIE) (No. 1415181752).

Appendix A. Supporting information

Supplementary data associated with this article can be found in the online version at doi:10.1016/j.pacs.2023.100456.

References

[1] V. Gray-Schopfer, C. Wellbrock, R. Marais, Melanoma biology and new targeted therapy, Nature 445 (7130) (2007) 851–857.
[2] P. Carli, V. De Giorgi, B. Giannotti, Dermoscopy and early diagnosis of melanoma: the light and the dark, Arch. Dermatol. 137 (12) (2001) 1641–1644.
[3] T. Mendonca, A.R. Marcal, A. Vieira, J.C. Nascimento, M. Silveira, J.S. Marques, J. Rozeira, Comparison of segmentation methods for automatic diagnosis of dermoscopy images. 2007 29th Annual International Conference of the IEEE Engineering in Medicine and Biology Society, IEEE,, 2007, pp. 6572–6575.
[4] G. Pellacani, A.M. Cesinaro, S. Seidenari, In vivo assessment of melanocytic nests in nevi and melanomas by reflectance confocal microscopy, Mod. Pathol. 18 (4) (2005) 469–474.
[5] G. Pellacani, P. Guitera, C. Longo, M. Avramidis, S. Seidenari, S. Menzies, The impact of in vivo reflectance confocal microscopy for the diagnostic accuracy of melanoma and equivocal melanocytic lesions, J. Invest. Dermatol. 127 (12) (2007) 2759–2765.
[6] T. Gambichler, P. Regeniter, F.G. Bechara, A. Orlikov, R. Vasa, G. Moussa, M. Stucker, P. Altmeyer, K. Hoffmann, Characterization of benign and malignant melanocytic skin lesions using optical coherence tomography in vivo, J. Am. Acad. Dermatol. 57 (4) (2007) 629–637.
[7] A. Rajabi-Estarabadi, J.M. Bittar, C. Zheng, V. Nascimento, I. Camacho, L.G. Feun, M. Nasiriavanaki, M. Kunz, K. Nouri, Optical coherence tomography imaging of melanoma skin cancer, Lasers Med Sci. 34 (2) (2019) 411–420.
[8] M.E. Vestergaard, P. Macaskill, P.E. Holt, S.W. Menzies, Dermoscopy compared with naked eye examination for the diagnosis of primary melanoma: a meta-analysis of studies performed in a clinical setting, Br. J. Dermatol. 159 (3) (2008) 669–676.
[9] R.M. Bakos, T.P. Blumetti, R. Roldan-Marin, G. Salerni, Noninvasive imaging tools in the diagnosis and treatment of skin cancers, Am. J. Clin. Dermatol. 19 (Suppl 1) (2018) 3–14.
[10] A.B.E. Attia, G. Balasundaram, M. Moothanchery, U.S. Dinish, R. Bi, V. Ntziachristos, M. Olivo, A review of clinical photoacoustic imaging: current and future trends, Photoacoustics 16 (2019), 100144.
[11] D. Seong, S. Yi, S. Han, J. Lee, S. Park, Y.-H. Hwang, J. Kim, H.K. Kim, M. Jeon, Target ischemic stroke model creation method using photoacoustic microscopy with simultaneous vessel monitoring and dynamic photothrombosis induction, Photoacoustics (2022), 100376.
[12] O. Abeyakoon, R. Woitek, M. Wallis, P. Moyle, S. Morscher, N. Dahlhaus, S. Ford, N. Burton, R. Manavaki, I. Mendichovszky, An optoacoustic imaging feature set to characterise blood vessels surrounding benign and malignant breast lesions, Photoacoustics 27 (2022), 100383.
[13] E. Alchera, M. Monieri, M. Maturi, I. Locatelli, E. Locatelli, S. Tortorella, A. Sacchi, A. Corti, M. Nebuloni, R. Lucianò, Early diagnosis of bladder cancer by photoacoustic imaging of tumor-targeted gold nanorods, Photoacoustics 28 (2022), 100400.
[14] V.P. Zharov, E.I. Galanzha, E.V. Shashkov, N.G. Khlebtsov, V.V. Tuchin, In vivo photoacoustic flow cytometry for monitoring of circulating single cancer cells and contrast agents, Opt. Lett. 31 (24) (2006) 3623–3625.
[15] E.I. Galanzha, E.V. Shashkov, P.M. Spring, J.Y. Suen, V.P. Zharov, In vivo, noninvasive, label-free detection and eradication of circulating metastatic melanoma cells using two-color photoacoustic flow cytometry with a diode laser, Cancer Res. 69 (20) (2009) 7926–7934.
[16] D.A. Nedosekin, M. Sarimollaoglu, J.H. Ye, E.I. Galanzha, V.P. Zharov, In Vivo Ultra-Fast Photoacoustic Flow Cytometry of Circulating Human Melanoma Cells Using Near-Infrared High-Pulse Rate Lasers, Cytom. Part A 79a (10) (2011) 825–833.
[17] Y. He, L. Wang, J. Shi, J. Yao, L. Li, R. Zhang, C.H. Huang, J. Zou, L.V. Wang, In vivo label-free photoacoustic flow cytography and on-the-spot laser killing of single circulating melanoma cells, Sci. Rep. 6 (1) (2016) 39616.
[18] E.I. Galanzha, M.S. Kokoska, E.V. Shashkov, J.W. Kim, V.V. Tuchin, V.P. Zharov, In vivo fiber-based multicolor photoacoustic detection and photothermal purging of metastasis in sentinel lymph nodes targeted by nanoparticles, Wiley Online Library, 2009.
[19] Y. Wang, K. Maslov, Y. Zhang, S. Hu, L. Yang, Y. Xia, J. Liu, L.V. Wang, Fiber-laser-based photoacoustic microscopy and melanoma cell detection, J. Biomed. Opt. 16 (1) (2011), 011014.
[20] C. Zhang, K.I. Maslov, J. Yao, L.V. Wang, In vivo photoacoustic microscopy with 7.6-μm axial resolution using a commercial 125-MHz ultrasonic transducer, J. Biomed. Opt. 17 (11) (2012), 116016.
[21] D.J. Grootendorst, J. Jose, M.W. Wouters, H. van Boven, J. Van der Hage, T.G. Van Leeuwen, W. Steenbergen, S. Manohar, T.J. Ruers, First experiences of photoacoustic imaging for detection of melanoma metastases in resected human lymph nodes, Lasers Surg. Med 44 (7) (2012) 541–549.
[22] J. Kim, Y.H. Kim, B. Park, H.M. Seo, C.H. Bang, G.S. Park, Y.M. Park, J.W. Rhie, J. H. Lee, C. Kim, Multispectral ex vivo photoacoustic imaging of cutaneous melanoma for better selection of the excision margin, Br. J. Dermatol. 179 (3) (2018) 780–782.
[23] H.F. Zhang, K. Maslov, G. Stoica, L.V. Wang, Functional photoacoustic microscopy for high-resolution and noninvasive in vivo imaging, Nat. Biotechnol. 24 (7) (2006) 848–851.
[24] J.T. Oh, M.L. Li, H.F. Zhang, K. Maslov, G. Stoica, L.V. Wang, Three-dimensional imaging of skin melanoma in vivo by dual-wavelength photoacoustic microscopy, J. Biomed. Opt. 11 (3) (2006) 34032.
[25] J. Staley, P. Grogan, A.K. Samadi, H. Cui, M.S. Cohen, X. Yang, Growth of melanoma brain tumors monitored by photoacoustic microscopy, J. Biomed. Opt. 15 (4) (2010), 040510.
[26] C. Kim, E.C. Cho, J. Chen, K.H. Song, L. Au, C. Favazza, Q. Zhang, C.M. Cobley, F. Gao, Y. Xia, L.V. Wang, In vivo molecular photoacoustic tomography of melanomas targeted by bioconjugated gold nanocages, ACS Nano 4 (8) (2010) 4559–4564.
[27] C. Zhang, K. Maslov, L.V. Wang, Subwavelength-resolution label-free photoacoustic microscopy of optical absorption in vivo, Opt. Lett. 35 (19) (2010) 3195–3197.
[28] Y. Zhou, W. Xing, K.I. Maslov, L.A. Cornelius, L.V. Wang, Handheld photoacoustic microscopy to detect melanoma depth in vivo, Opt. Lett. 39 (16) (2014) 4731–4734.
[29] Y. Zhou, G. Li, L.R. Zhu, C.Y. Li, L.A. Cornelius, L.H.V. Wang, Handheld photoacoustic probe to detect both melanoma depth and volume at high speed in vivo, J. Biophoton. 8 (11–12) (2015) 961–967.
[30] Z. Xu, Y. Pan, N. Chen, S. Zeng, L. Liu, R. Gao, J. Zhang, C. Fang, L. Song, C. Liu, Visualizing tumor angiogenesis and boundary with polygon-scanning multiscale photoacoustic microscopy, Photoacoustics 26 (2022), 100342.
[31] Z. Jiang, Y. Ding, J.F. Lovell, Y. Zhang, Design and application of organic contrast agents for molecular imaging in the second near infrared (NIR-II) window, Photoacoustics (2022), 100426.
[32] A.M. Smith, M.C. Mancini, S. Nie, Bioimaging: second window for in vivo imaging, Nat. Nanotechnol. 4 (11) (2009) 710–711.
[33] G.P. Luke, D. Yeager, S.Y. Emelianov, Biomedical applications of photoacoustic imaging with exogenous contrast agents, Ann. Biomed. Eng. 40 (2) (2012) 422–437.
[34] A.B.E. Attia, S.Y. Chuah, D. Razansky, C.J.H. Ho, P. Malempati, U.S. Dinish, R. Bi, C.Y. Fu, S.J. Ford, J.S. Lee, M.W.P. Tan, M. Olivo, S.T.G. Thng, Noninvasive real-

time characterization of non-melanoma skin cancers with handheld optoacoustic probes, Photoacoustics 7 (2017) 20–26.
[35] Y. Wang, D. Xu, S. Yang, D. Xing, Toward in vivo biopsy of melanoma based on photoacoustic and ultrasound dual imaging with an integrated detector, Biomed. Opt. Express 7 (2) (2016) 279–286.
[36] Z. Chen, E. Rank, K.M. Meiburger, C. Sinz, A. Hodul, E. Zhang, E. Hoover, M. Minneman, J. Ensher, P.C. Beard, H. Kittler, R.A. Leitgeb, W. Drexler, M. Liu, Non-invasive multimodal optical coherence and photoacoustic tomography for human skin imaging, Sci. Rep. 7 (1) (2017) 17975.
[37] F. Salin, C.L. Blanc, J. Squier, C. Barty, Thermal eigenmode amplifiers for diffraction-limited amplification of ultrashort pulses, Opt. Lett. 23 (9) (1998) 718–720.
[38] C.S. Rao, S. Kundu, A.K. Ray, High repetition rate nanosecond optical parametric oscillator pumped by the third harmonic of a DPSSL, Appl. Phys. B-Lasers Opt. 124 (8) (2018) 1–8.
[39] B. Park, M. Han, J. Park, T. Kim, H. Ryu, Y. Seo, W.J. Kim, H.H. Kim, C. Kim, A photoacoustic finder fully integrated with a solid-state dye laser and transparent ultrasound transducer, Photoacoustics 23 (2021), 100290.
[40] J. Ahn, J.W. Baik, Y. Kim, K. Choi, J. Park, H. Kim, J.Y. Kim, H.H. Kim, S.H. Nam, C. Kim, Fully integrated photoacoustic microscopy and photoplethysmography of human in vivo, Photoacoustics (2022), 100374.
[41] J. Ahn, J.Y. Kim, W. Choi, C. Kim, High-resolution functional photoacoustic monitoring of vascular dynamics in human fingers, Photoacoustics 23 (2021), 100282.
[42] M. Chen, X. Duan, B. Lan, T. Vu, X. Zhu, Q. Rong, W. Yang, U. Hoffmann, J. Zou, J. Yao, High-speed functional photoacoustic microscopy using a water-immersible two-axis torsion-bending scanner, Photoacoustics 24 (2021), 100309.
[43] M. Chen, L. Jiang, C. Cook, Y. Zeng, T. Vu, R. Chen, G. Lu, W. Yang, U. Hoffmann, Q. Zhou, High-speed wide-field photoacoustic microscopy using a cylindrically focused transparent high-frequency ultrasound transducer, Photoacoustics 28 (2022), 100417.
[44] S.-W. Cho, S.M. Park, B. Park, T.G. Lee, B.-M. Kim, C. Kim, J. Kim, S.-W. Lee, C.-S. Kim, High-speed photoacoustic microscopy: A review dedicated on light sources, Photoacoustics 24 (2021), 100291.
[45] T. Vu, A. DiSpirito III, D. Li, Z. Wang, X. Zhu, M. Chen, L. Jiang, D. Zhang, J. Luo, Y. S. Zhang, Deep image prior for undersampling high-speed photoacoustic microscopy, Photoacoustics 22 (2021), 100266.
[46] K. Wang, C. Li, R. Chen, J. Shi, Recent advances in high-speed photoacoustic microscopy, Photoacoustics 24 (2021), 100294.
[47] J. Chen, Y. Zhang, S. Bai, J. Zhu, P. Chirarattananon, K. Ni, Q. Zhou, L. Wang, Dual-foci fast-scanning photoacoustic microscopy with 3.2-MHz A-line rate, Photoacoustics 23 (2021), 100292.
[48] Y.N. Billeh, M.Y. Liu, T. Buma, Spectroscopic photoacoustic microscopy using a photonic crystal fiber supercontinuum source, Opt. Express 18 (18) (2010) 18519–18524.
[49] C. Lee, S. Han, S. Kim, M. Jeon, M.Y. Jeon, C. Kim, J. Kim, Combined photoacoustic and optical coherence tomography using a single near-infrared supercontinuum laser source, Appl. Opt. 52 (9) (2013) 1824–1828.
[50] M.K. Dasa, G. Nteroli, P. Bowen, G. Messa, Y. Feng, C.R. Petersen, S. Koutsikou, M. Bondu, P.M. Moselund, A. Podoleanu, A. Bradu, C. Markos, O. Bang, All-fibre supercontinuum laser for in vivo multispectral photoacoustic microscopy of lipids in the extended near-infrared region, Photoacoustics 18 (2020), 100163.
[51] C. Lee, M. Jeon, M.Y. Jeon, J. Kim, C. Kim, In vitro photoacoustic measurement of hemoglobin oxygen saturation using a single pulsed broadband supercontinuum laser source, Appl. Opt. 53 (18) (2014) 3884–3889.
[52] M.R. Ferrari, J.L. Farland, T. Buma, Photoacoustic microscopy using four-wave mixing in a multimode fiber. 2015 IEEE International Ultrasonics Symposium (IUS), IEEE, 2015, pp. 1–4.
[53] M.M. Bondu, C.D. Brooks, C. Jakobsen, K. Oakes, P.M. Moselund, L. Leick, O. Bang, A. Podoleanu, High energy supercontinuum sources using tapered photonic crystal fibers for multispectral photoacoustic microscopy, J. Biomed. Opt. 21 (6) (2016), 061005.
[54] E. Aytac-Kipergil, A. Demirkiran, N. Uluc, S. Yavas, T. Kayikcioglu, S. Salman, S. G. Karamuk, F.O. Ilday, M.B. Unlu, Development of a fiber laser with independently adjustable properties for optical resolution photoacoustic microscopy, Sci. Rep. 6 (1) (2016) 1–10.
[55] X. Shu, M. Bondu, B. Dong, A. Podoleanu, L. Leick, H.F. Zhang, Single all-fiber-based nanosecond-pulsed supercontinuum source for multispectral photoacoustic microscopy and optical coherence tomography, Opt. Lett. 41 (12) (2016) 2743–2746.
[56] M. Bondu, M.J. Marques, P.M. Moselund, G. Lall, A. Bradu, A. Podoleanu, Multispectral photoacoustic microscopy and optical coherence tomography using a single supercontinuum source, Photoacoustics 9 (2018) 21–30.
[57] T. Buma, N.C. Conley, S.W. Choi, Multispectral photoacoustic microscopy of lipids using a pulsed supercontinuum laser, Biomed. Opt. Express 9 (1) (2018) 276–288.
[58] Y. Chang, Y.C. Hu, Z.J. Chen, D. Xing, Co-impulse multispectral photoacoustic microscopy and optical coherence tomography system using a single supercontinuum laser, Opt. Lett. 44 (18) (2019) 4459–4462.
[59] T. Hirasawa, K. Tachi, M. Miyashita, S. Okawa, T. Kushibiki, M. Ishihara, Spectroscopic photoacoustic microscopic imaging during single spatial scan using broadband excitation light pulses with wavelength-dependent time delay, Photoacoustics 26 (2022), 100364.
[60] D. Koeplinger, M. Liu, T. Buma, Photoacoustic microscopy with a pulsed multi-color source based on stimulated Raman scattering. 2011 IEEE International Ultrasonics Symposium, IEEE, 2011, pp. 296–299.
[61] A.K. Loya, J. Dumas, T. Buma, Photoacoustic microscopy with a tunable source based on cascaded stimulated Raman scattering in a large-mode area photonic crystal fiber. 2012 IEEE International Ultrasonics Symposium, IEEE, 2012, pp. 1208–1211.
[62] P. Hajireza, A. Forbrich, R.J. Zemp, Multifocus optical-resolution photoacoustic microscopy using stimulated Raman scattering and chromatic aberration, Opt. Lett. 38 (15) (2013) 2711–2713.
[63] P. Hajireza, A. Forbrich, R. Zemp, In-Vivo functional optical-resolution photoacoustic microscopy with stimulated Raman scattering fiber-laser source, Biomed. Opt. Express 5 (2) (2014) 539–546.
[64] T. Buma, J.L. Farland, M.R. Ferrari, Near-infrared multispectral photoacoustic microscopy using a graded-index fiber amplifier, Photoacoustics 4 (3) (2016) 83–90.
[65] Y. Liang, L. Jin, B.O. Guan, L. Wang, 2 MHz multi-wavelength pulsed laser for functional photoacoustic microscopy, Opt. Lett. 42 (7) (2017) 1452–1455.
[66] N.Q. Bui, S.W. Cho, M.S. Moorthy, S.M. Park, Z. Piao, S.Y. Nam, H.W. Kang, C. S. Kim, J. Oh, In vivo photoacoustic monitoring using 700-nm region Raman source for targeting Prussian blue nanoparticles in mouse tumor model, Sci. Rep. 8 (1) (2018) 1–9.
[67] S.-W. Cho, H. Kang, S.M. Park, G. Lim, Z. Piao, S.-W. Lee, C.-S. Kim, T.G. Lee, Optimal generation of ten individual green-to-red Raman source for wavelength-dependent real-time OR-PAM images, IEEE J. Sel. Top. Quantum Electron. 25 (1) (2018) 1–9.
[68] S.M. Park, D.Y. Kim, S.W. Cho, B.M. Kim, T.G. Lee, C.S. Kim, S.W. Lee, Quickly alternating green and red laser source for real-time multispectral photoacoustic microscopy, Photoacoustics 20 (2020), 100204.
[69] H. Lee, M.R. Seeger, N. Lippok, S.K. Nadkarni, G. van Soest, B.E. Bouma, Nanosecond SRS fiber amplifier for label-free near-infrared photoacoustic microscopy of lipids, Photoacoustics 25 (2022), 100331.
[70] G.P. Agrawal, Nonlinear Fiber Optics-Agrawal.
[71] S. Jacques, Optical Absorption of Melanin, 1998.
[72] S. Prahl, Optical Absorption of Hemoglobin, 1999.
[73] G.M. Hale, M.R. Querry, Optical constants of water in the 200-nm to 200-μm wavelength region, Appl. Opt. 12 (3) (1973) 555–563.
[74] J. Gröhl, M. Schellenberg, K. Dreher, L. Maier-Hein, Deep learning for biomedical photoacoustic imaging: A review, Photoacoustics 22 (2021), 100241.
[75] D. Seong, E. Lee, Y. Kim, S. Han, J. Lee, M. Jeon, J. Kim, Three-dimensional reconstructing undersampled photoacoustic microscopy images using deep learning, Photoacoustics (2022), 100429.
[76] R. Buczynski, Photonic crystal fibers, Acta Phys. Pol. A 106 (2) (2004) 141–167.
[77] H. Pourbeyram, G.P. Agrawal, A. Mafi, Stimulated Raman scattering cascade spanning the wavelength range of 523 to 1750 nm using a graded-index multimode optical fiber, Appl. Phys. Lett. 102 (20) (2013), 201107.
[78] A.K. Abeeluck, C. Headley, Continuous-wave pumping in the anomalous-and normal-dispersion regimes of nonlinear fibers for supercontinuum generation, Opt. Lett. 30 (1) (2005) 61–63.
[79] J.Y. Kim, C. Lee, K. Park, S. Han, C. Kim, High-speed and high-SNR photoacoustic microscopy based on a galvanometer mirror in non-conducting liquid, Sci. Rep. 6 (1) (2016) 1–7.
[80] J. Chen, Y. Zhang, L. He, Y. Liang, L. Wang, Wide-field polygon-scanning photoacoustic microscopy of oxygen saturation at 1-MHz A-line rate, Photoacoustics 20 (2020), 100195.
[81] N.T.P. Truong, J. Choi, S. Park, C.D. Ly, S.-W. Cho, S. Mondal, H.G. Lim, C.-S. Kim, J. Oh, Ultra-widefield photoacoustic microscopy with a dual-channel slider-crank laser-scanning apparatus for in vivo biomedical study, Photoacoustics 23 (2021), 100274.
[82] T.T.V. Phan, N.Q. Bui, S.W. Cho, S. Bharathiraja, P. Manivasagan, M.S. Moorthy, S. Mondal, C.S. Kim, J. Oh, Photoacoustic imaging-guided photothermal therapy with tumor-targeting HA-FeOOH@PPy nanorods, Sci. Rep. 8 (1) (2018) 1–13.
[83] S. Cho, J. Baik, R. Managuli, C. Kim, 3D PHOVIS: 3D photoacoustic visualization studio, Photoacoustics 18 (2020), 100168.
[84] E.A. Grice, H.H. Kong, G. Renaud, A.C. Young, N.C.S. Program, G.G. Bouffard, R. W. Blakesley, T.G. Wolfsberg, M.L. Turner, J.A. Segre, A diversity profile of the human skin microbiota, Genome Res 18 (7) (2008) 1043–1050.
[85] W. Wadsworth, N. Joly, J. Knight, T. Birks, F. Biancalana, P. Russell, Supercontinuum and four-wave mixing with Q-switched pulses in endlessly single-mode photonic crystal fibres, Opt. Express 12 (2) (2004) 299–309.
[86] S. Coen, A.H.L. Chau, R. Leonhardt, J.D. Harvey, J.C. Knight, W.J. Wadsworth, P.S. J. Russell, Supercontinuum generation by stimulated Raman scattering and parametric four-wave mixing in photonic crystal fibers, J. Opt. Soc. Am. B-Opt. Phys. 19 (4) (2002) 753–764.
[87] J.M. Dudley, L. Provino, N. Grossard, H. Maillotte, R.S. Windeler, B.J. Eggleton, S. Coen, Supercontinuum generation in air-silica microstructured fibers with nanosecond and femtosecond pulse pumping, J. Opt. Soc. Am. B-Opt. Phys. 19 (4) (2002) 765–771.
[88] A. Kudlinski, V. Pureur, G. Bouwmans, A. Mussot, Experimental investigation of combined four-wave mixing and Raman effect in the normal dispersion regime of a photonic crystal fiber, Opt. Lett. 33 (21) (2008) 2488–2490.

Soon-Woo Cho received M.S. and Ph.D. degrees from the Department of Cogno-Mechatronics Engineering, Pusan National University, South Korea, in 2016 and 2022, respectively. She is currently working at Engineering Research Center for Color-modulated Extra-sensory Perception Technology, Pusan National University as a postdoctoral researcher. Her current research interests include the development of high-speed fiber laser for multimodal imaging systems including photoacoustic imaging and optical coherence tomography.

Thi Tuong Vy Phan completed a doctorate in 2019 at Department of Biomedical Engineering, Pukyong National University, Busan, South Korea. In her doctorate studies, she especially focused on the biomaterial and nanomaterial preparation for photo-based therapies. Since Mar 2019, she has worked as a researcher and lecturer at the Institute of Research and Development, Duy Tan University, Vietnam. Her research interests are the development of environmental-friendly methods for nanomaterial preparation and the application of marine-derived biomaterial study in biomedical field.

Van Tu Nguyen Van Tu Nguyen obtained the B.S. degree in Biomedical Engineering from Hanoi University of Science and Technology, Vietnam in 2015. He worked as specialist engineer at GE HealthCare's distributor, in Hanoi, Vietnam for 1 year. The, he received the M.S. degree and Ph.D. degree in Biomedical Engineering from Pukyong National University, Busan, South Korea, in 2018 and 2022, respectively. He currently joins as a Post-doc Fellow at Biomedical Engineering Department, Duke University, Durham, NC, USA. His research focuses on biomedical imaging methods, including photoacoustic imaging and fluorescence imaging.

Sang Min Park received the M.S. degree from the Department of Cogno-Mechatronics Engineering, Pusan National University, Busan, South Korea, in 2018. He is currently working toward the Ph.D. degree at the Department of Cogno-Mechatronics Engineering, Pusan National University. His current research interests include the development of nonlinear fiber laser and optical imaging system for biomedical applications.

Hwidon Lee received his PhD degree in the Department of Cogno-Mechatronics Engineering at Pusan National University, South Korea, in 2015. He is currently working at Massachusetts General Hospital and Harvard Medical School as a Research Fellow (2019). His current research interests are the developments of novel light sources for biomedical applications including optical coherence tomography and photoacoustic imaging.

Junghwan Oh received the B.S. degree in Mechanical engineering from Pukyong National University in 1992, and the M. S. and Ph.D. degrees in Biomedical engineering from The University of Texas at Austin, USA, in 2003 and 2007, respectively. In 2010, he joined the Department of Biomedical Engineering at Pukyong National University, where he is a Full Professor. He also serves as Director of OhLabs Corporation research center. His current research interests include ultrasonic-based diagnostic imaging modalities for biomedical engineering applications, biomedical signal processing and health care systems.

Chang-Seok Kim received the Ph.D. degree from The Johns Hopkins University, Baltimore, MD, USA, in 2004. He is a Professor with the Department of Optics and Mechatronics Engineering and the Department of Cogno-Mechatronics Engineering, Pusan National University, Busan, South Korea. His current research interests include the development of novel fiber laser systems and application of them into biomedical, telecommunication, and sensor areas.